Electronic Supplementary Material (ESI) for Materials Chemistry Frontiers.

Experimental section

Synthesis of iron-containing complex nanoflakes. Iron-containing complex nanoflakes were synthesized via a facile hydrothermal method. Both 0.5927 g of $FeCl_3 \cdot 6H_2O$ and 1.5916 g of urea were dissolved in 70 mL of ethylene glycol under magnetic stirring at room temperature for 30 min to form a solution, which was then transferred into a 100 mL Teflon-lined stainless steel autoclave and heated at 180 °C for 8 h. After cooling at room temperature, the precipitates were collected by centrifugation, washed several times with ethanol, and dried at 60 °C for 24 h in an oven.

Synthesis of 2D-Fe_3O_4/C nanoflakes. Iron-containing complex nanoflakes were annealed in a nitrogen atmosphere at 400, 450, and 500 °C for 2 h with a heating rate of 5 °C min^{-1}, and denoted as 2D-Fe_3O_4/C-400, 2D-Fe_3O_4/C-450, and 2D-Fe_3O_4/C-500, respectively.

Synthesis of NiCo-LDHs. First, ZIF-67 nanoparticles were synthesized as the precursor of NiCo-LDHs. After that, the as-prepared ZIF-67 nanoparticles were transformed to NiCo-LDH nanosheets in accordance with the precedent of the previous report.[S1] Briefly, 120 mg of ZIF-67 and 480 mg of $Ni(NO_3)_2 \cdot 6H_2O$ were dissolved in a mixed solvent comprised of 120 mL of ethanol and 30 mL of deionized water under magnetic stirring for 30 min; the solution was then sealed in a Teflon-lined autoclave and heated at 90 °C for 1 h. NiCo-LDHs were obtained by centrifugation, washed several times with absolute ethanol, and then dried in an oven at 60 °C for 24 h.

Characterization. The morphologies and structural details of the samples were examined by field-emission scanning electron microscopy (FESEM, Hitachi S-4800) and transmission electron microscopy (TEM, JEOL-2010). The phase and crystallographic structures of the samples were investigated by X-ray diffraction (XRD, Rigaku, Ultima IV with D/teX Ultra) using Cu Ka radiation in a range of 10° to 90° with a scan speed of 5° min^{-1}. The chemical elemental compositions of the materials were measured by X-ray photoelectron spectrometer (XPS, Axis Ultra, Kratos Analytical Ltd.). Thermogravimetric analysis (TGA) was performed using a Shimadzu-50 thermoanalyzer from room temperature to 900 ^{o}C at a ramp rate of 10 ^{o}C min^{-1} in air. The Brunauer-Emmett-Teller (BET) specific surface areas and Barrett–Joyner–Halenda (BJH) pore-size distributions were obtained from the nitrogen physical adsorption-desorption isotherms at 77 K using an Autosorb iQ2 analyzer (Quantachrome Instruments).

Electrochemical measurements. Working electrodes were fabricated by mixing 80 wt.% of active material, 10 wt.% of carbon black, and 10 wt.% of polyvinylidene fluoride in N-methyl-2-pyrrolidone solution. The slurries were coated onto graphite substrates, which were then dried at 120 °C for 12 h under vacuum conditions.

The electrochemical measurements were carried out in a three-electrode system in 2 M KOH aqueous solution for supercapacitors and 1 M NaCl aqueous solution for CDI. The as-prepared electrode materials, an Ag/AgCl electrode, and platinum foil were used as the working electrode, reference electrode, and counter electrode, respectively. The electrochemical performance of the as-synthesized material electrodes was studied using cyclic voltammetry (CV), electrochemical impedance spectroscopy (EIS) at 0.1 Hz - 100 kHz and 5 mV AC amplitude, and galvanostatic charge-discharge (GCD) on an AUTO-LAB PGSTAT 204N electrochemical workstation.

The specific capacitance (C_s, F g^{-1}) was calculated from the GCD process with the following equation:

$$C_S = I \times \Delta t/(m \times \Delta V)\,, \tag{S1}$$

where I and Δt represent the discharge current (A) and discharge time (s), respectively; and, m and ΔV are the mass of active material (g) and the potential window during the discharge process, respectively.

Supercapacitor measurements. For the preparation of gel electrolytes, 2 g of polyvinyl alcohol (PVA) was first dissolved in 20 mL of deionized water under stirring at 85 °C for 4 h to form solution A. Second, 3.366 g of KOH was added to 10 mL of deionized water to form solution B. Then, solution B was added into solution A drop by drop. Afterward, the electrolyte was placed under low temperature conditions until the gel solidified.[S2] Finally, the hybrid supercapacitor was assembled by using the 2D-Fe_3O_4/C-450 electrode as the negative electrode and NiCo-LDHs as the positive electrode using a PVA-KOH gel as a solid-state electrolyte.

The energy density (E, W h kg^{-1}) and power density (P, W kg^{-1}) were obtained as follows:

$$E = C_S \times \Delta V^2/7.2, \tag{S2}$$

$$P = 3600 \times E/\Delta t, \tag{S3}$$

where Cs, ΔV, and Δt are the specific capacitance (F g^{-1}), potential window (V), and discharge time (s), respectively.

CDI measurements. Desalination experiments were carried out using a batch-mode CDI unit under constant recycling in 500 mg L^{-1} NaCl solution. The mass of the active material, Fe_3O_4/C-450 was 0.046 g. Ion exchange membranes were used to suppress the co-ion expulsion. During the desalination process, the flow rate, temperature, and volume were kept at 100 mL min^{-1}, 298 K, and 80 mL, respectively. Furthermore, the conductivity of the NaCl solution was monitored by using a conductivity meter (DDS-308, Precision and Scientific Instrument). The desalination capacity (Γ, mg g^{-1}) was calculated according to previous reports:[S3,S4]

$$\Gamma = \frac{(C_0 - C_t) \times V}{m}, \tag{S4}$$

where C_0 and C_t are the NaCl concentrations (*i.e.*, half of the NaCl solution's conductivity) at the initial stage and t time (mg L^{-1}), respectively, V is the volume of the NaCl solution (L), and m is the mass of active materials (g).

Supplementary Figures and Tables

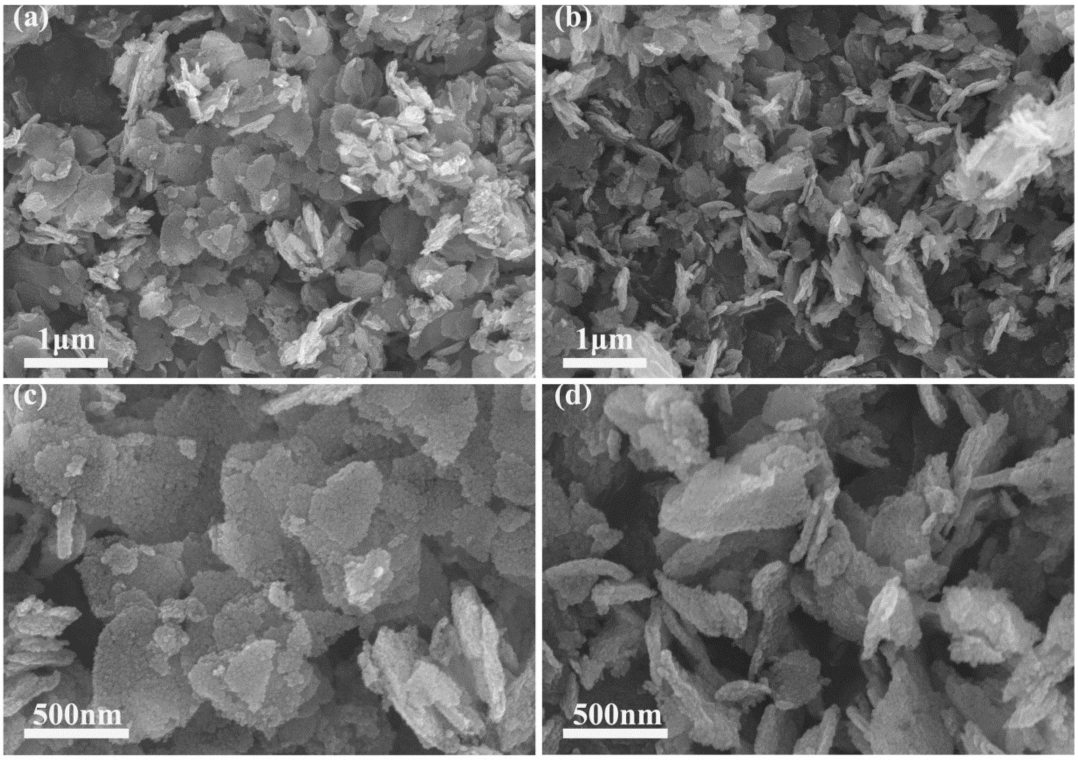

Fig. S1 (a, b) Low- and (c, d) high-resolution FESEM images of (a, c) 2D-Fe_3O_4/C-400 and (b, d) 2D-Fe_3O_4/C-500 at different magnifications.

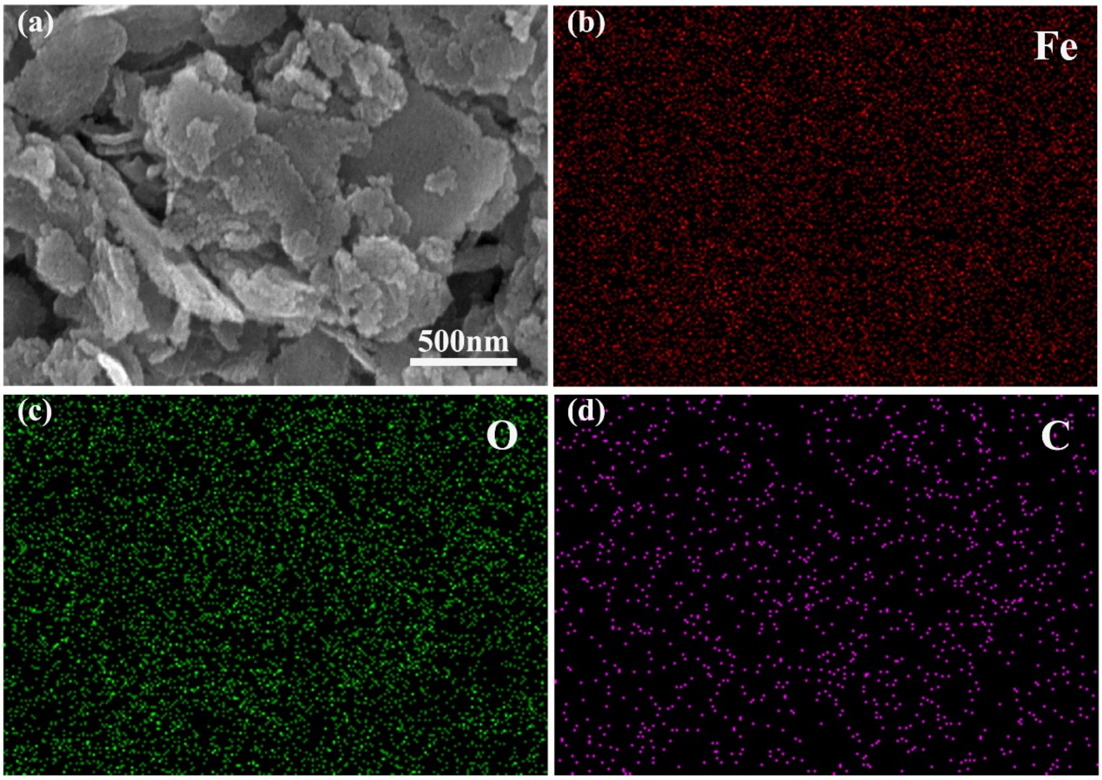

Fig. S2 (a) FESEM and (b–d) corresponding elemental mapping images of 2D-Fe_3O_4/C-450.

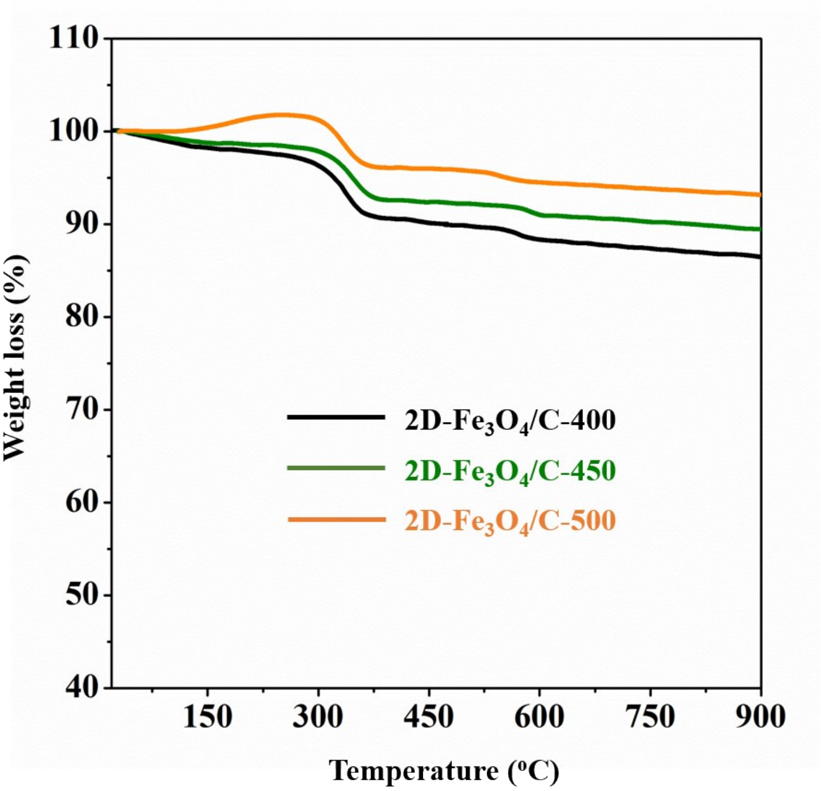

Fig. S3 TGA curves of all 2D-Fe_3O_4/C samples.

Supplementary Note for Fig. S3: We assume that the weight ratio of carbon is x, so the weight ratio of Fe_3O_4 (molar mass: 231.54 g/mol) in the composite is 1-x. As we all know, after annealing 2D-Fe_3O_4/C samples in air, the final product will be Fe_2O_3 (molar mass: 159.69 g/mol), which will refer to a weight ratio of 239.54×(1-x)/231.54. Based on the results of TGA curves (**Fig. S3**), the remaining weight ratios of all 2D-Fe_3O_4/C samples are 89.49, 92.59, and 96.40 wt.% for 2D-Fe_3O_4/C-400, 2D-Fe_3O_4/C-450, and 2D-Fe_3O_4/C-500, respectively. Therefore, the corresponding mass ratios of carbon in 2D-Fe_3O_4/C-400, 2D-Fe_3O_4/C-450, and 2D-Fe_3O_4/C-500 are 13.5, 10.5, and 6.82 wt.%, respectively.

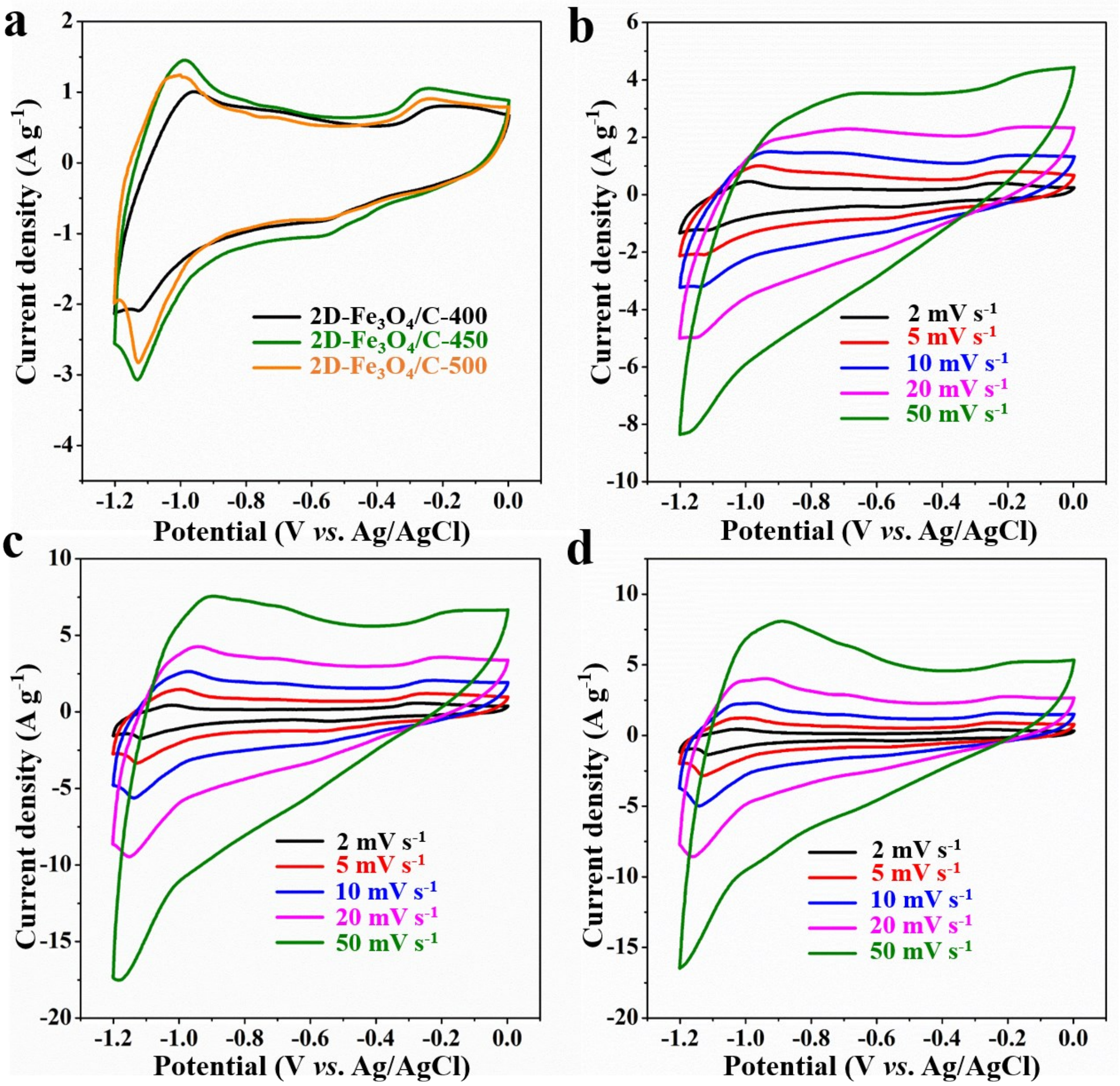

Fig. S4 (a) CV curves for 2D-Fe_3O_4/C-400, 2D-Fe_3O_4/C-450, and 2D-Fe_3O_4/C-500 electrodes at 5 mV s^{-1}; CV curves of (b) 2D-Fe_3O_4/C-400, (c) 2D-Fe_3O_4/C-450, and (d) 2D-Fe_3O_4/C-500 at various scan rates.

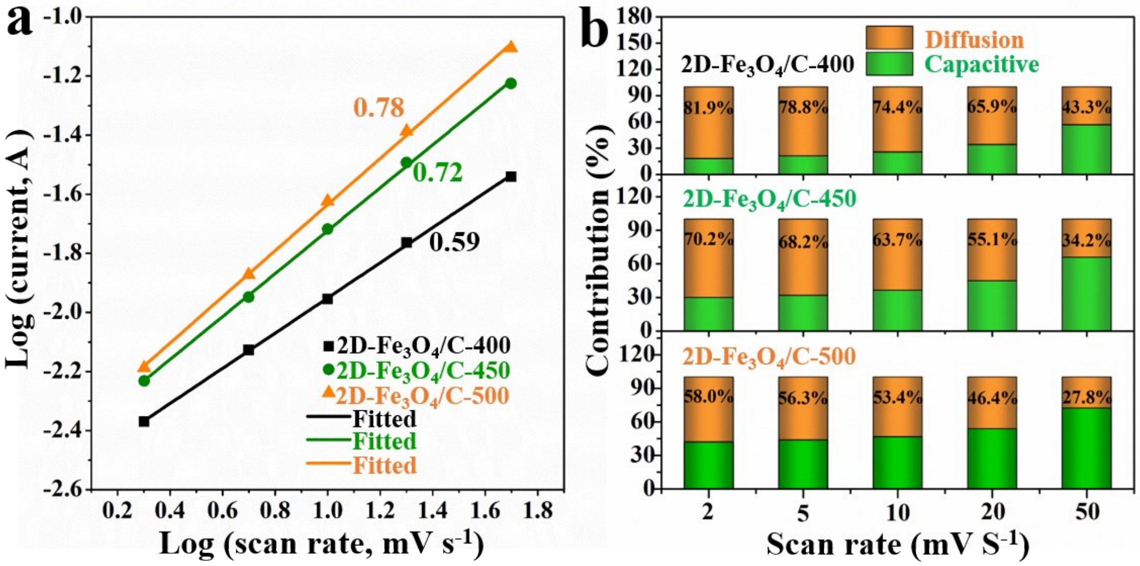

Fig. S5 (a) Linear relationship for log(i, anodic peak current) *versus* log(v, scan rate) of different samples; (b) ratios of capacitive and diffusion-controlled contributions at different scan rates.

Supplementary Notes for Figs S4–5:

To further explore the capacitive behavior of the composites, the CV curves of the 2D-Fe_3O_4/C electrodes at scan rates from 2 to 50 mV s^{-1} in 2 M KOH electrolyte are shown in **Fig. S4b–d**. The proportion of diffusion-controlled contribution and surface-controlled capacitive contribution are calculated using the following equation:

$$i = av^b, \tag{S5}$$

where i and v are the corresponding currents at a certain voltage (A) and scan rate in CV measurements (mV s^{-1}), respectively; a and b are adjustable values. When the b value equals 0.5, a diffusion-controlled process is indicated, whereas the b value is close to 1, which suggests a capacitive-controlled behavior.[40] **Fig. S5a** shows the profiles regarding log(i) *versus* log(v) of the 2D-Fe_3O_4/C composites, and the calculated b values are 0.59, 0.72, and 0.78, implying that the electrochemical behaviors of the 2D-Fe_3O_4/C composite are dominated by both surface-controlled capacitive effects and diffusion-controlled processes. The diffusion-controlled and capacitive contributions can be calculated by the following equation:

$$i = k_1 v + k_2 v^{1/2}, \tag{S6}$$

where $k_1 v$ and $k_2 v^{1/2}$ correspond to the currents at a certain voltage controlled by capacitive behavior and diffusion-controlled process, respectively. As shown in **Fig. S5b**, the diffusion-controlled process dominates the electrochemical behaviors at lower scan rates, especially in the 2D-Fe_3O_4/C-400 and 2D-Fe_3O_4/C-450 electrodes, and with the increase of scan rates, the surface-controlled capacitive contributions of 2D-Fe_3O_4/C samples increase. In addition, an interesting phenomenon has also been observed, that is, with the decrease of carbon content in the sample from 2D-Fe_3O_4/C-400 and 2D-Fe_3O_4/C-450 to 2D-Fe_3O_4/C-500, the surface-controlled capacitive contributions are enhanced accordingly. This might be due to following reasons: as discussed in a previous paper titled "Definitions of pseudocapacitive materials: a brief review (*Energy & Environmental Materials*, 2 (2019): 30–37), it is hard to ascribe all of the surface-controlled capacitive contribution to the electrochemical double-layer capacitive effects, since the fast redox reactions and the ion intercalation/de-intercalation that happened at the surface can also contribute to the surface-controlled current response, especially in a system using ultrafine-sized nanomaterials. In other words, since our 2D-Fe_3O_4/C nanoflakes are composed of numerous Fe_3O_4 nanoparticles with sizes of 10–20 nm, we cannot ignore the presence of redox reactions or ion intercalation/de-intercalation behavior at the surface. Thus, although the carbon content decreases, the capacitive contribution still increases.

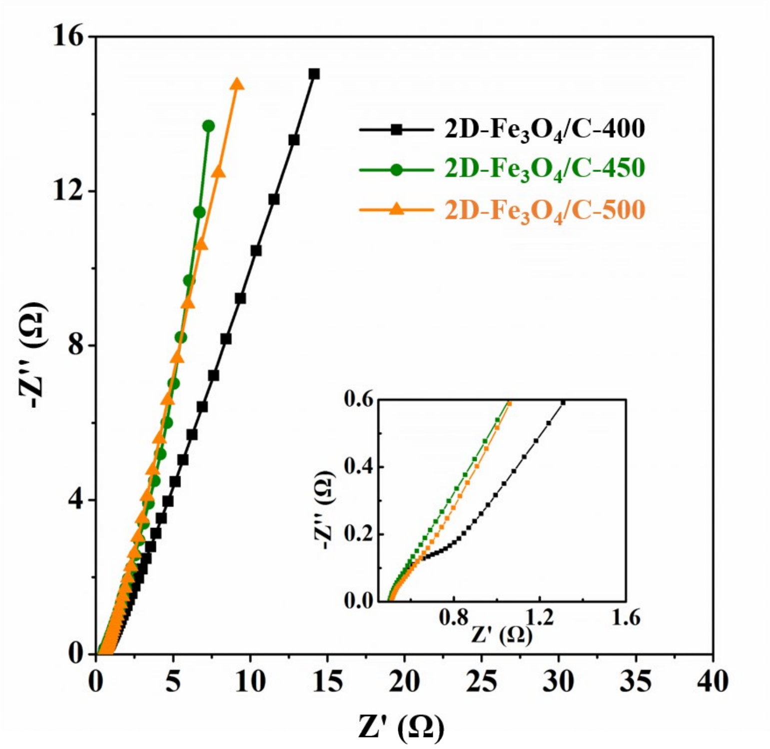

Fig. S6 Nyquist plots of 2D-Fe_3O_4/C samples. Insets show the corresponding magnified spectra in the high-frequency region and the equivalent circuit model.

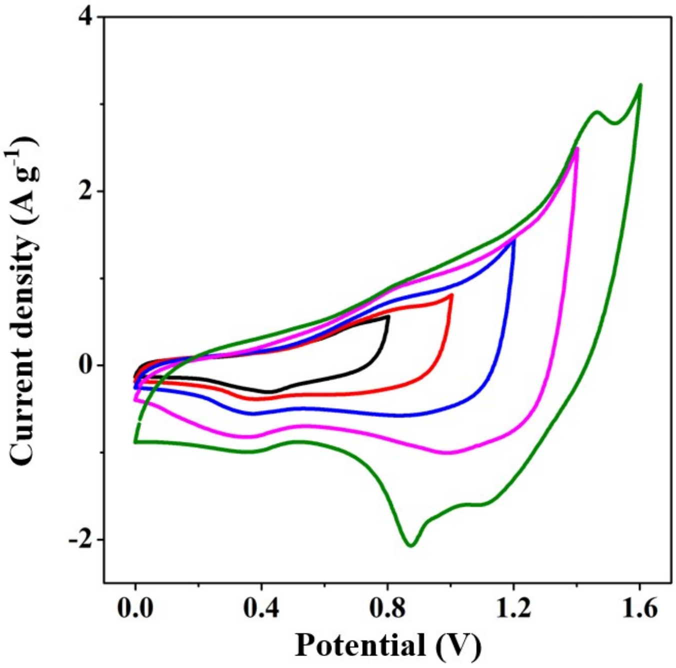

Fig. S7 CV curves for the Fe_3O_4/C-450//NiCo-LDHs asymmetrical system with varying operation windows in 2 M KOH at 10 mV s^{-1}.

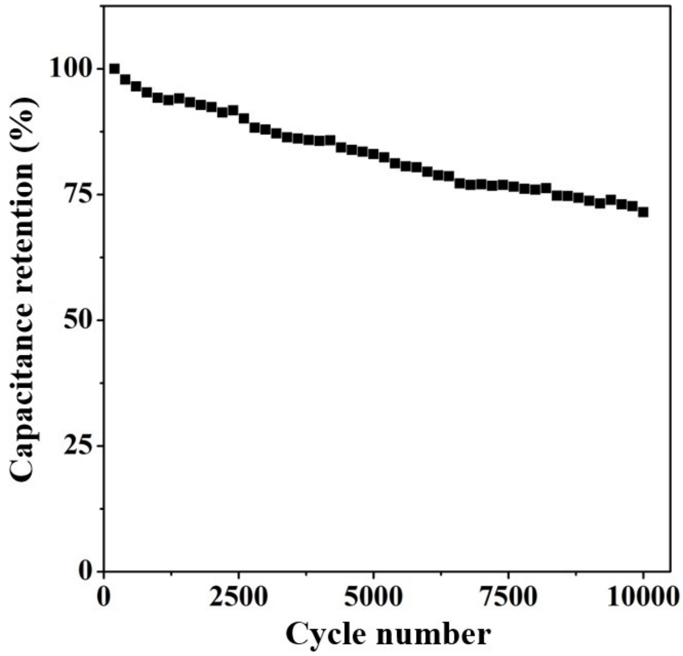

Fig. S8 Cycling capacitance retention of a hybrid supercapacitor.

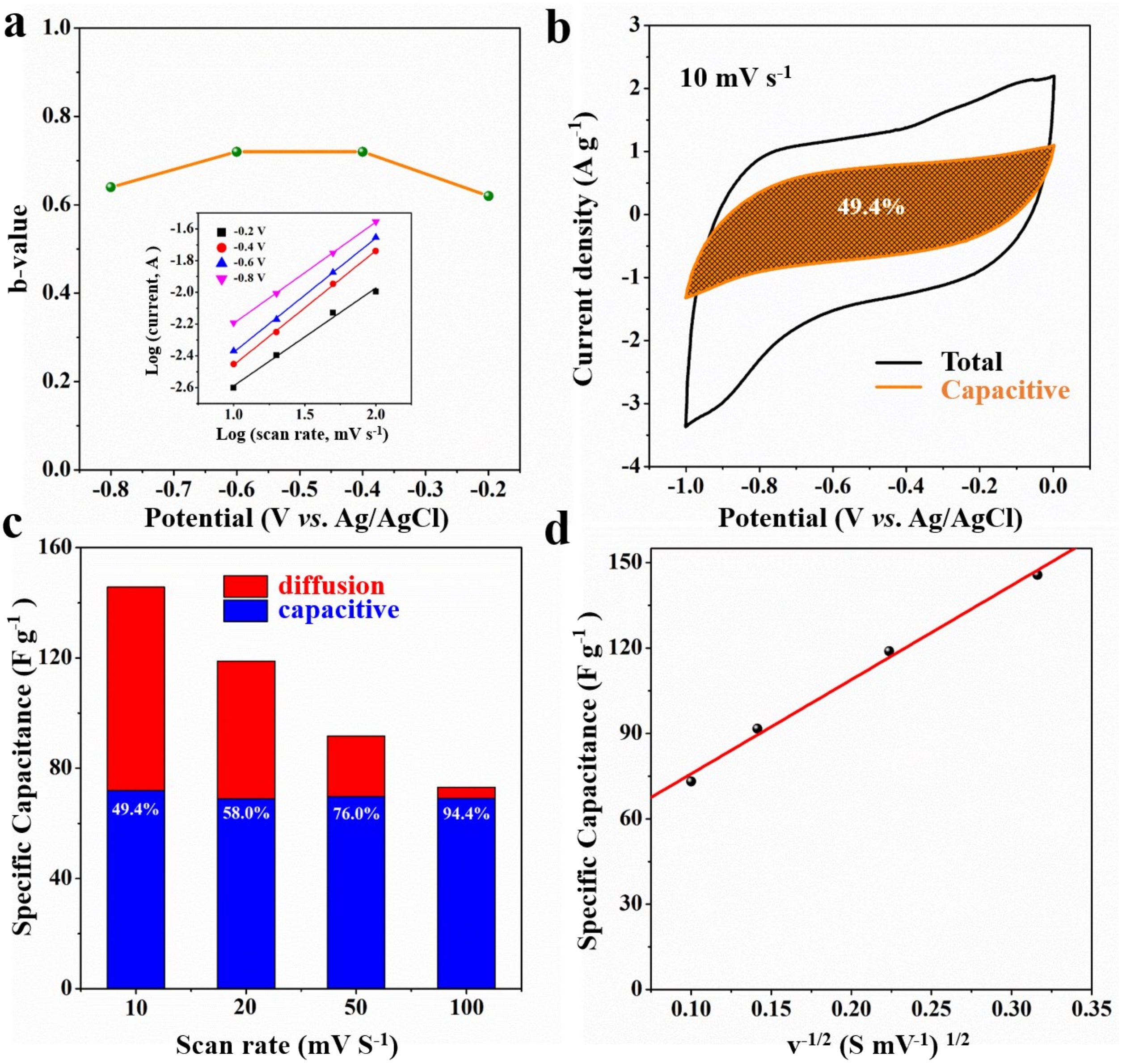

Fig. S9 (a) Curve of b-values versus potential; (b) illustration of capacitive and total contributions at 10 mV s^{-1}; (c) separate capacitances at varying scan rates; (d) relationships of specific capacitances *versus* the square root of the scan rate; Inset of (a) Linear relationship for log(*i*, current) *versus* log(*v*, scan rate) at different potentials.

Supplementary Note for Fig. S9d: The current response at a fixed potential could be expressed as following equation:

$$i(V) = k_1 v + k_2 v^{1/2}, \qquad \text{(S7)}$$

wherein $k_1 v$ and $k_2 v^{1/2}$ correspond to the current contributions from surface-controlled charging and diffusion-controlled Na ion-insertion processes, respectively.

According to the relationship between the total capacitance (C, F g^{-1}) and the current i(V):

$$C = \int i(V)dV \big/ 2mv\Delta V, \qquad \text{(S8)}$$

where m is the mass of the electrode (g), and v is the scan rate, C could be further expressed as the total of the capacitances from the surface-controlled charging contribution (C_1, F g^{-1}), *i.e.*, $\int(k_1v)dV/2mv\Delta V$, and the diffusion-controlled Na ion-insertion process (C_2, F g^{-1}), referring to $\int(k_2v^{1/2})dV/2mv\Delta V$, which is displayed in the following formula:

$$C = \int (k_1v)dV\big/2mv\Delta V + \int (k_2v^{1/2})dV\big/2mv\Delta V. \qquad \text{(S9)}$$

This formula can be further simplified as:

$$C = \int k_1dV\big/2m\Delta V + \int k_2dV\big/2mv^{1/2}\Delta V. \qquad \text{(S10)}$$

We therefore analyzed the correlation between C and $v^{1/2}$ and fitted the plots as shown in **Fig. S9d**. The intercept of the *y*-axis corresponds to the separate capacitance C_1 of the surface-controlled charging process. As calculated, the value is 67.5 F g^{-1}.

Table S1 Comparison of 2D-Fe_3O_4/C with other TMOs materials in CDI

Material	Voltage (V)	Desalination capacity (mg g^{-1})	Desalination time (min)	Mean desalination rate (mg g^{-1} min^{-1})	Reference
Ti-ACC	1.0	2.05	>180	<0.0115	S5
AC-TiO_2	1.2	~12.7	>200	<0.0635	S6
TiO_2/AC	1.2	8.05	>25	<0.322	S7
GA/TiO_2	1.2	15.1	>6.7	<2.265	S8
ACTNF	1.2	17.7	5	3.54	S9
TiO_2-coated AC	1.2	17	10	1.7	S10
RGO/TiO_2 nanorod	1.2	16.4	5	3.28	S11
TiO_2/CNTs	1.2	4.3	20	0.215	S12
THC-A	1.2	13.11	>40	<0.328	S13
MnO_2/NCs	1.2	0.99	50	0.0198	S14
MnO_2/PSS/CNTs	1.2	4.7	~25	~0.188	S15
CAGDMnAct	1.5	6.4	150	0.0427	S16
RGO–PPy–Mn	2.0	18.4	120	0.153	S17
MnO_2/MWCNTs	1.8	6.65	24	0.277	S18
MnO_2/AC	1.0	9.26	30	0.309	S19
MnO_2/CNT–CS	1.6	10.07	30	0.336	S20
ZnO–ACC	1.2	8.5	7.08	1.2	S21
ZnO/AC	1.2	9.4	40	0.235	S22
ZnO-coated ACC	1.5	5.72	6.8	0.841	S23
RGO@Fe_3O_4	1.2	~8.33	30	0.278	S24
Graphene/SnO_2	1.4	1.49	90	0.0166	S25
N-AC/SnO_2	1.2	3.42	1.83	2.052	S26
RGO-SnO_2	1.2	17.62	30	0.587	S27
ZrO_2 fibers/AC	1.2	16.35	30	0.545	S28
RuO_2(20)–AC	1.2	11.3	60	0.188	S29
rGO/Co_3O_4	1.6	20.21	30	0.674	S30
2D-Fe_3O_4/C-450	1.2	28.5	7.5	3.8	This work

References

(S1) P. Wang, Y. Li, S. Li, X. Liao, S. Sun, Water-promoted zeolitic imidazolate framework-67 transformation to Ni–Co layered double hydroxide hollow microsphere for supercapacitor electrode material, *J. Mater. Sci.: Mater. Electron.*, 2017, **28**, 9221-9227.

(S2) H. Fan, R. Niu, J. Duan, W. Liu, W. Shen, Fe_3O_4@Carbon Nanosheets for All-Solid-State Supercapacitor Electrodes, *ACS Appl. Mater. Interfaces*, 2016, **8**, 19475-19483.

(S3) X. Shen, Y. Xiong, R. Hai, F. Yu, J. Ma, All-MXene-Based Integrated Membrane Electrode Constructed using $Ti_3C_2T_x$ as an Intercalating Agent for High-Performance Desalination, *Environ. Sci. Technol.*, 2020, **54**, 4554-4563.

(S4) K. Wang, Y. Liu, Z. Ding, Y. Li, T. Lu, L. Pan, Metal–organic-frameworks-derived $NaTi_2(PO_4)_3$/carbon composites for efficient hybrid capacitive deionization, *J. Mater. Chem. A*, 2019, **7**, 12126-12133.

(S5) M.-W. Ryoo, J.-H. Kim, G. Seo, Role of titania incorporated on activated carbon cloth for capacitive deionization of NaCl solution, *J. Colloid Interface Sci.*, 2003, **264**, 414-419.

(S6) L.M. Chang, X.Y. Duan, W. Liu, Preparation and electrosorption desalination performance of activated carbon electrode with titania, *Desalination*, 2011, **270**, 285-290.

(S7) P.-I. Liu, L.-C. Chung, H. Shao, T.-M. Liang, R.-Y. Horng, C.-C.M. Ma, M.-C. Chang, Microwave-assisted ionothermal synthesis of nanostructured anatase titanium dioxide/activated carbon composite as electrode material for capacitive deionization, *Electrochim. Acta*, 2013, **96**, 173-179.

(S8) H. Yin, S. Zhao, J. Wan, H. Tang, L. Chang, L. He, H. Zhao, Y. Gao, Z. Tang, Three-dimensional graphene/metal oxide nanoparticle hybrids for high-performance capacitive deionization of saline water, *Adv. Mater.*, 2013, **25**, 6270-6276.

(S9) A.G. El-Deen, J.-H. Choi, K.A. Khalil, A.A. Almajid, N.A. Barakat, A TiO_2 nanofiber/activated carbon composite as a novel effective electrode material for capacitive deionization of brackish water, *RSC Adv.*, 2014, **4**, 64634-64642.

(S10) C. Kim, J. Lee, S. Kim, J. Yoon, TiO_2 sol–gel spray method for carbon electrode fabrication to enhance desalination efficiency of capacitive deionization, *Desalination*, 2014, **342**, 70-74.

(S11) A.G. El-Deen, J.-H. Choi, C.S. Kim, K.A. Khalil, A.A. Almajid, N.A. Barakat, TiO_2 nanorod-intercalated reduced graphene oxide as high performance electrode material for membrane capacitive deionization, *Desalination*, 2015, **361**, 53-64.

(S12) H. Li, Y. Ma, R. Niu, Improved capacitive deionization performance by coupling TiO_2 nanoparticles with carbon nanotubes, *Sep. Purif. Technol.*, 2016, **171**, 93-100.

(S13) K. Wei, Y. Zhang, W. Han, J. Li, X. Sun, J. Shen, L. Wang, A novel capacitive electrode based on TiO_2-NTs array with carbon embedded for water deionization: Fabrication, characterization and application study, *Desalination*, 2017, **420**, 70-78.

(S14) J. Yang, L. Zou, H. Song, Z. Hao, Development of novel MnO_2/nanoporous carbon composite electrodes in capacitive deionization technology, *Desalination*, 2011, **276**, 199-206.

(S15) J. Yang, L. Zou, H. Song, Preparing MnO_2/PSS/CNTs composite electrodes by layer-by-layer deposition of MnO_2 in the membrane capacitive deionisation, *Desalination*, 2012, **286**, 108-114.

(S16) M.C. Zafra, P. Lavela, G. Rasines, C. Macías, J.L. Tirado, C.O. Ania, A novel method for metal oxide deposition on carbon aerogels with potential application in capacitive deionization of saline water, *Electrochim. Acta*, 2014, **135**, 208-216.

(S17) X. Gu, Y. Yang, Y. Hu, M. Hu, J. Huang, C. Wang, Facile fabrication of graphene–polypyrrole–Mn composites as high-performance electrodes for capacitive deionization, *J. Mater. Chem. A*, 2015, **3**, 5866-5874.

(S18) B. Chen, Y. Wang, Z. Chang, X. Wang, M. Li, X. Liu, L. Zhang, Y. Wu, Enhanced capacitive desalination of MnO_2 by forming composite with multi-walled carbon nanotubes, *RSC Adv.*, 2016, **6**, 6730-6736.

(S19) Y.-H. Liu, H.-C. Hsi, K.-C. Li, C.-H. Hou, Electrodeposited Manganese Dioxide/Activated Carbon Composite As a High-Performance Electrode Material for Capacitive Deionization, *ACS Sustain. Chem. Eng.*, 2016, **4**, 4762-4770.

(S20) Y.-H. Liu, T.-C. Yu, Y.-W. Chen, C.-H. Hou, Incorporating Manganese Dioxide in Carbon Nanotube–Chitosan as a Pseudocapacitive Composite Electrode for High-Performance Desalination, *ACS Sustain. Chem. Eng.*, 2018, **6**, 3196-3205.

(S21) M.T.Z. Myint, S.H. Al-Harthi, J. Dutta, Brackish water desalination by capacitive deionization using zinc oxide micro/nanostructures grafted on activated carbon cloth electrodes, *Desalination*, 2014, **344**, 236-242.

(S22) J. Liu, M. Lu, J. Yang, J. Cheng, W. Cai, Capacitive desalination of ZnO/activated carbon asymmetric capacitor and mechanism analysis, *Electrochim. Acta*, 2015, **151**, 312-318.

(S23) K. Laxman, D. Kimoto, A. Sahakyan, J. Dutta, Nanoparticulate Dielectric Overlayer for Enhanced Electric Fields in a Capacitive Deionization Device, *ACS Appl. Mater. Interfaces*, 2018, **10**, 5941-5948.

(S24) H. Li, Z.Y. Leong, W. Shi, J. Zhang, T. Chen, H.Y. Yang, Hydrothermally synthesized graphene and Fe_3O_4 nanocomposites for high performance capacitive deionization, *RSC Adv.*, 2016, **6**, 11967-11972.

(S25) A.G. El-Deen, N.A.M. Barakat, K.A. Khalil, M. Motlak, H. Yong Kim, Graphene/SnO_2 nanocomposite as an effective electrode material for saline water desalination using capacitive deionization, *Ceram. Int.*, 2014, **40**, 14627-14634.

(S26) A.S. Yasin, J. Jeong, I.M.A. Mohamed, C.H. Park, C.S. Kim, Fabrication of N-doped &SnO_2-incorporated activated carbon to enhance desalination and bio-decontamination performance for capacitive deionization, *J. Alloys Compd.*, 2017, **729**, 764-775.

(S27) S.K. Sami, J.Y. Seo, S.-E. Hyeon, M.S.A. Shershah, P.-J. Yoo, C.-H. Chung, Enhanced capacitive deionization performance by an rGO–SnO_2 nanocomposite modified carbon felt electrode, *RSC Adv.*, 2018, **8**, 4182-4190.

(S28) A.S. Yasin, M. Obaid, Ibrahim M.A. Mohamed, A. Yousef, N.A.M. Barakat, ZrO_2 nanofibers/activated carbon composite as a novel and effective electrode material for the enhancement of capacitive deionization performance, *RSC Adv.*, 2017, **7**, 4616-4626.

(S29) X. Ma, Y.-A. Chen, K. Zhou, P.-C. Wu, C.-H. Hou, Enhanced desalination performance via mixed capacitive-Faradaic ion storage using RuO_2-activated carbon composite electrodes, *Electrochim. Acta*, 2019, **295**, 769-777.

(S30) G. Divyapriya, K.K. Vijayakumar, I. Nambi, Development of a novel graphene/Co_3O_4 composite for hybrid capacitive deionization system, *Desalination*, 2019, **451**, 102-110.